Turbulence Measurements in Blade Tip Vortices Using Dual-Plane Particle Image Velocimetry

Bradley Johnson* Manikandan Ramasamy† J. Gordon Leishman‡

Department of Aerospace Engineering
Glenn L. Martin Institute of Technology
University of Maryland, College Park, MD 20742

Abstract

The mean and turbulent flow characteristics of the blade tip vortices generated by a hovering rotor were studied using dual-plane stereoscopic digital particle image velocimetry (DPS-DPIV). The DPS-DPIV technique permitted the non-invasive measurement of the three components of the unsteady velocity field, and the nine components of the velocity gradient tensor. DPS-DPIV is based on coincident flow measurements made over two differentially-spaced laser sheet planes, thus allowing for velocity gradient calculations to be made also in a direction orthogonal to the measurement planes. A polarization-based technique employing beam-splitting optical cubes and filters was used to give the two laser sheets orthogonal polarizations, and to ensure that the cameras imaged Mie scattered light from only one or other of the laser sheets. The digital processing of the images used a deformation grid correlation algorithm, optimized for the high velocity gradients and small-scale turbulent flows found inside vortices. Detailed turbulence measurements were used to derive the fluctuating terms that are involved in the Reynolds-averaged stress transport equations. The results have shown that the turbulence distribution is anisotropic, and that the stress in the flow cannot be represented as a linear function of its strain. The measurement of all nine velocity gradients also allowed for precise measurements of the vorticity vector, as well as the inclination between the vortex axis and the measurement plane. This inclination was found to be almost orthogonal at all early wake ages.

* NDSEG Fellow. **bjo212@umd.edu**
† Assistant Research Scientist. **mani@umd.edu**
‡ Minta Martin Professor. **leishman@umd.edu**
Presented at the 34th European Rotorcraft Forum, Arena and Convention Center, Liverpool, England, September 16–19, 2008. © 2008 by Johnson, Ramasamy & Leishman. All rights reserved. Published by the Royal Aeronautical Society of Great Britain with permission.

Nomenclature

A	rotor disk area
c	blade chord
C_T	rotor thrust coefficient, $= T/\rho A\Omega^2 R^2$
$\hat{i}, \hat{j}, \hat{k}$	unit directional vectors
$\vec{n}$	vector normal to measurement plane
p	static pressure
r, θ, z	polar coordinate system
r_c	core radius of the tip vortex
r_0	initial core radius of the tip vortex
R	radius of blade
Ri	Richardson's number
Re_v	vortex Reynolds number, $= \Gamma_v/\nu$
u, v, w	velocities in Cartesian coordinates
$\overline{u'}$, $\overline{v'}$, $\overline{w'}$	normalized RMS velocities (Cartesian)
$\overline{u'v'}$	normalized Reynolds stress in X,Y plane
$\overline{v'w'}$	normalized Reynolds stress in Y,Z plane
$\overline{u'w'}$	normalized Reynolds stress in X,Z plane
V_r, V_θ	radial and swirl velocities of the tip vortex
$\overline{V_r'}$, $\overline{V_\theta'}$, $\overline{V_z'}$	normalized RMS velocities
V_{tip}	tip speed of blade
x, y, z	vortex coordinate system (Cartesian)
X, Y, Z	DPIV coordinate system (Cartesian)
α	Lamb's constant, = 1.25643
Γ_v	total vortex circulation, $= 2\pi r V_\theta$
δ	ratio of apparent to actual kinematic viscosity
δ_{ij}	Kronecker delta
θ	inclination between $\vec{n}$ and the vortex axis
θ_{MP}	inclination between laser sheet and vortex axis
ν	kinematic viscosity
ζ	wake age
ρ	air density
σ	strain
τ	stress
ψ	azimuthal position of blade
$\vec{\omega}$	vorticity vector
Ω	rotational speed of the rotor
2-C	two-component
3-C	three-component

Introduction

Decades of research has led to a better understanding of the complex vortical wakes generated by rotor blades (e.g., Refs. 1–10), and in the assessment of the effects of the wake on vehicle performance, unsteady airloads, vibration, and noise. Much research has been focused on better understanding the blade tip vortices, which are the dominant features of a rotor wake (e.g., Refs. 11–16). It is important to better measure the factors that determine the formation, strength, and trajectories of these tip vortices, so as to develop better validated mathematical models for describing the rotor aerodynamics. To this end, no such model can be completely successful unless it is able to accurately represent the three-dimensional, turbulent flows inside the vortices. There are currently very few measurements of such turbulent flow properties.

Predictions of rotor wake developments using computational fluid dynamics (CFD) based on Navier–Stokes (N–S) methods are becoming increasingly more successful. Most of the efforts have been focused in solving the Reynolds-Averaged Navier–Stokes (RANS) equations. RANS methods represent a time-averaged form of the N–S equations, in which the flow velocity u_i at a point is represented as a combination of a mean component $\overline{u_i}$ and a fluctuating component u_i', as given by

$$u_i = \overline{u_i} + u_i' \tag{1}$$

Using Eq. 1 results in the RANS equations, as given by

$$\frac{D\overline{u_i}}{Dt} = \frac{\partial}{\partial x_j}\left[-\frac{\overline{p}\,\delta_{ij}}{\rho} + \nu\left(\frac{\partial \overline{u_i}}{\partial x_j} + \frac{\partial \overline{u_j}}{\partial x_i}\right) - \overline{u_i' u_j'}\right] \tag{2}$$

where D/Dt is the substantial derivative, and the overbar in each case represents the time-averaged or mean values.

Time-averaging the N–S equations to form the RANS equations bypasses the need to explicitly compute the high-frequency, small-scale fluctuations caused by turbulent eddies in the flow (i.e., the u_i' and u_j' terms). However, this advantage is countered by the creation of additional unknown terms in Eq. 2, i.e., the Reynolds stresses $\overline{u_i' u_j'}$. These terms make the RANS equations unsolvable unless a closure model is used to rebalance the number of equations and unknowns. These "correlation terms" basically account for the effects of turbulent velocity fluctuations created by the presence of eddies of various length scales. All such closure models are based on actual flow measurements, so the model adopted must be consistent with the flow physics so as to correctly model the contributions of turbulence to the developing flow. Because different turbulence models must be developed for different types of physical problems and types of flows, the models will understandably vary in complexity and in the number of equations and closure coefficients that are needed (e.g., Refs. 17–21). Generally, these coefficients are derived from measurements in free shear or homogenous flows, and not vortex flows.

The objective of the present work was to undertake specific types of flow measurements to give a better understanding of the turbulence production, transport, and diffusion in the rotor wake, and more specifically, inside the blade tip vortices. This goal required velocity field measurements with high spatial and temporal resolution, and was accomplished using digital particle image velocimetry (DPIV). Specifically, a dual-plane DPIV technique (DPS-DPIV) was developed to simultaneously measure the mean and turbulent flow velocities, the six in-plane velocity gradients, and the three out-of-plane gradients.

Description of the Experiment

The present study involved the use of a dual-plane stereo digital particle image velocimetry (DPS-DPIV) system. Two coupled DPIV systems comprising of a stereo pair of 4 mega-pixel CCD cameras and a single 2 mega-pixel CCD camera were used to measure simultaneously the flow velocities over two parallel, adjacent planes that were situated in the wake of a small-scale rotor system. The wake flow was uniformly seeded with a thermally produced mineral oil fog, which comprised of particles of nominally 0.2 microns in diameter; these particles were small enough to minimize particle tracking errors (Ref. 22).

Rotor System

A single bladed rotor operated in hover was used for the measurements. The advantages of the single bladed rotor included the ability to create and study a helicoidal vortex filament without interference from other vortices and turbulence in the flow that would be generated by other blades (Ref. 23). A single helicoidal vortex is also much more spatially and temporally stable than systems of multiple vortices (Ref. 24). This simpler rotor configuration allowed for the vortex flow to be studied to much older wake ages without the higher levels of aperiodicity that are typically encountered when using multi-bladed rotors.

The single blade was of rectangular planform, untwisted, with a radius of 406 mm (16 inches) and chord of 44.5 mm (1.752 inches), and was balanced with a counterweight. The NACA 2415 airfoil was used. The blade tip speed was 89.28 m/s (292.91 ft/s), giving a tip Mach number and chord Reynolds number of 0.26 and 272,000, respectively. All the tests were made at an effective blade loading coefficient of $C_T/\sigma \approx 0.064$ using a collective pitch of 4.5° (measured from the chord line).

DPS-DPIV Requirements and Setup

DPS-DPIV differs from conventional DPIV because it can measure all nine components of the velocity gradient tensor, in addition to the three unsteady flow components. The flow velocity gradient tensor can be written as

$$\nabla V = \begin{bmatrix} \partial u/\partial x & \partial u/\partial y & \partial u/\partial z \\ \partial v/\partial x & \partial v/\partial y & \partial v/\partial z \\ \partial w/\partial x & \partial w/\partial y & \partial w/\partial z \end{bmatrix} \quad (3)$$

A conventional, stereoscopic (3-component) DPIV system can measure three components of velocity in a given plane (Refs. 25–28), but only six of the nine velocity gradient tensor components in Eq. 3. Estimating the velocity gradients in the out-of-plane direction (i.e., finding the $\partial/\partial z$ terms in Eq. 3) with DPIV requires the measurement of three components of velocity in at least two planes that are parallel to each other and are separated by a small spatial distance in the z direction.

DPS-DPIV Imaging Arrangement

The optical setup of the current DPS-DPIV system is shown in Fig. 1. Two coupled DPIV systems with two light sheet planes were required to simultaneously measure the flow velocities from the Mie scattering of the seed particles passing through both laser sheet planes. Three dual Nd-YAG lasers with 110 mJ/pulse were used, the third laser being used to image the flow in regions where the blade cast a shadow from the other lasers. The third laser prevented the need to mosaic the resulting flow images and ensured coincidence of the measurements.

A DPS-DPIV system can be arranged as a combination of two stereoscopic DPIV systems, or as a combination of one stereoscopic 3-C DPIV system and one 2-C DPIV system (Refs. 29, 30). While the former combination provides directly all the three components of velocity in both of the two parallel planes, the latter system provides all the three components of velocity in one plane and only the in-plane velocities (i.e., two components) in the other plane. The out-of-plane velocities are then calculated using the assumption of mass conservation in the flow (Ref. **?**). This latter method provides several advantages over the dual-plane arrangement with two stereoscopic systems, mainly because it is somewhat simpler to set up and has lower instrumentation costs. An in-situ calibration procedure was used to determine the relationships between the two-dimensional image planes and three-dimensional object fields for both position mapping and 3-C velocity field reconstruction (see later).

The present setup is shown in Fig. 1. The conventional 2-C DPIV configuration (the 2 mega-pixel camera is labeled as C2 in Fig. 1) is used to measure two components of flow velocity in one plane, while a stereo setup (a pair

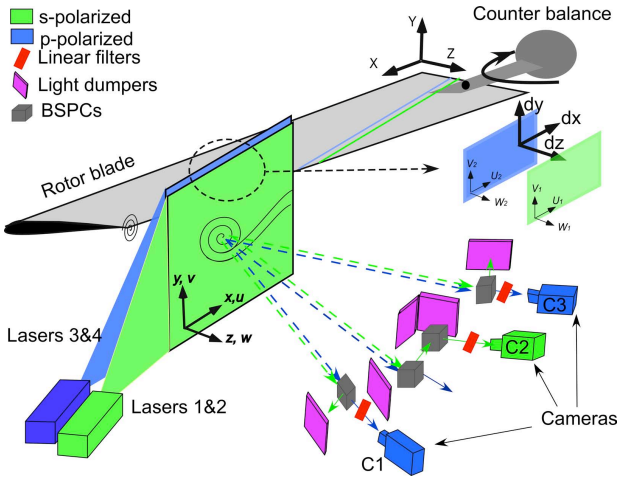

(a) Schematic of the DPS-DPIV setup

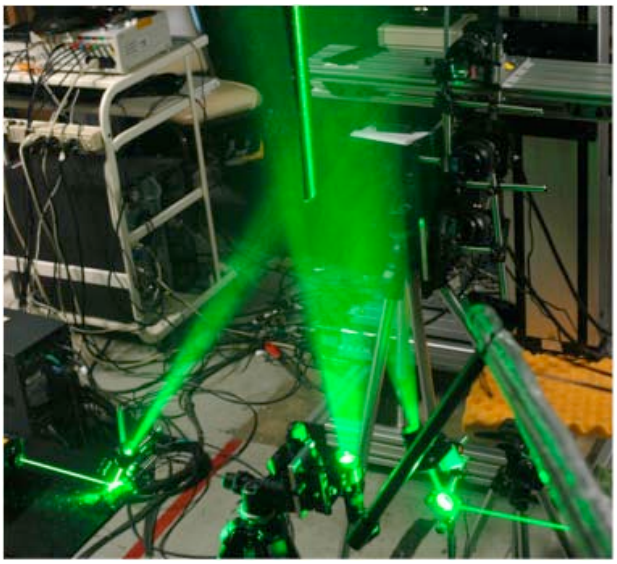

(b) Three dual Nd-YAG lasers illuminating the flow

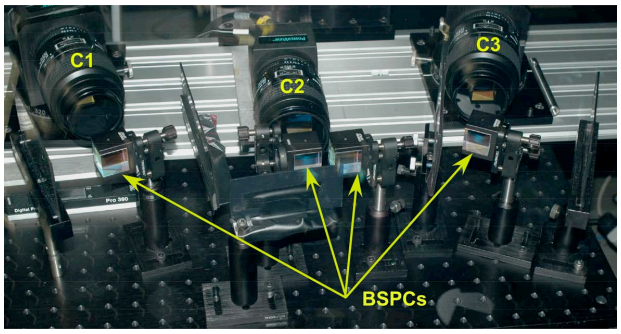

(c) Close-up of CCD cameras and beam-splitting cubes

Figure 1: Schematic and photographs of the DPS-DPIV system as used for the rotor wake studies: (a) Schematic, (b) Lasers used to image the flow, (c) Close-up of cameras and beam-splitting cubes.

of 4 mega-pixel cameras labeled C1 and C3 in Fig. 1) is used to measure the three flow velocity components in the plane of the second laser sheet. The stereo cameras satisfied the Scheimpflug condition. Mass conservation in the form of Eq. 4 was applied to estimate the third component of velocity in the 2-C measurement plane (shown in green) by using the incompressible flow equation

$$w_1 = -\left(\frac{\Delta u_1}{\Delta x} + \frac{\Delta v_1}{\Delta y}\right)\Delta z + w_2 \qquad (4)$$

The resulting velocity fields that are measured in the two respective planes (Fig. 2) can then be analyzed to determine all nine components of the velocity gradient tensor.

However, to maintain accuracy with these velocity gradient calculations, several precautions have to be taken. In terms of the set up procedures, the two laser light sheets must be both parallel and adjacent to each other, ideally just a few millimeters apart. Additionally, the two lasers must be synchronized in phase, not only with each other, but also with both sets of cameras and precisely to the rotational frequency of the rotor.

Each laser pair, i.e., lasers 1 & 2 and lasers 3 & 4 shown in Fig. 1(a), delivers two sheet pulses with a separation time of 2 μs. The first pulse from the green pair (laser 1) is synchronized with the first pulse from the blue pair (laser 3), and the same for the second pulse from each laser pair (lasers 2 & 4). In the timing circuit, each of the three cameras must then be synchronized with the lasers

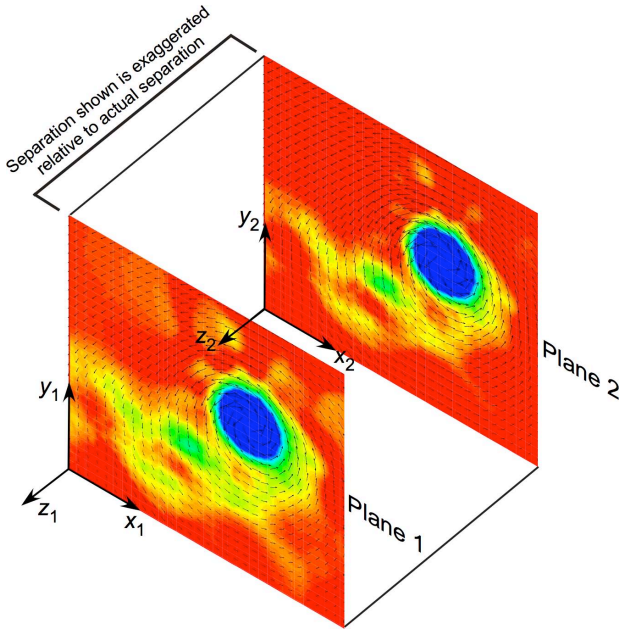

Figure 2: Typical instantaneous velocity fields measured using DPS-DPIV. Interplane separation is exaggerated; actual plane separation is much smaller than the vector-to-vector spacing within each plane.

(i.e., the first particle pair image in each plane is captured upon the firing of lasers 1 & 3 and the second image in each plane is captured during the firing of lasers 2 & 4).

Crosstalk and Laser Polarization

There are several challenges in making simultaneous flow measurements in spatially adjacent, parallel laser planes, mainly resulting from imaging crosstalk between the cameras. Crosstalk, which has its source from Mie scattering from seed particles in both illuminated laser planes, will occur because each camera has a finite depth of field. If any camera images both laser planes, not only will its planar velocity map be erroneous after DPIV processing, but the comparison between the velocity map in the first plane with that of the second plane (which is needed to calculate velocity gradients in the z direction) would be meaningless. This problem is heightened by the need to have the intensity of each laser set to high levels so that sufficient Mie scattering can be captured by all cameras with approximately the same levels of intensity.

To guarantee that each respective set of cameras only images the flow in its designated laser sheet plane, the special optical setup shown in Fig. 1 was used. The purpose was to split the polarizations of the two respective laser pairs, and then to use appropriate filters and beam-splitting optical cubes placed in front of each camera to guarantee that they only imaged one type of polarized light. Notice that lasers 1 & 2 are s-polarized, and lasers 3 & 4 are p-polarized. In the present setup, the center 2-C camera (C2) was tuned to the s-polarization of lasers 1 & 2, and the stereo cameras (C1 & C3) were tuned to the p-polarized light from lasers 3 & 4.

Figure 1(a) shows how the Mie scattered blue (i.e., p-polarized) and green (i.e., s-polarized) light come from each respective laser sheet. A beam-splitting cube in front of the 2-C camera initially images both sets of images, and allows the p-polarized blue light to pass through directly but redirects the s-polarized green light to a second beam-splitting cube. This second cube redirects the s-polarized light into the camera; a linear filter over the lens acts as a final buffer against any stray p-polarized light.

Each stereo camera also has one beam-splitting cube placed in front of it; these cubes redirect the s-polarized light into separate light dumps but allow the p-polarized blue light to pass through to the camera. Each stereo camera has a linear filter over the lens (oriented at a different angle to that of the 2-C camera) to act as a final buffer against any s-polarized light.

Final verification of the efficacy of this optical setup was made before measurements were started to ensure that the cameras saw only Mie scattering from their designated lasers (i.e., to ensure that there was absolutely no image crosstalk).

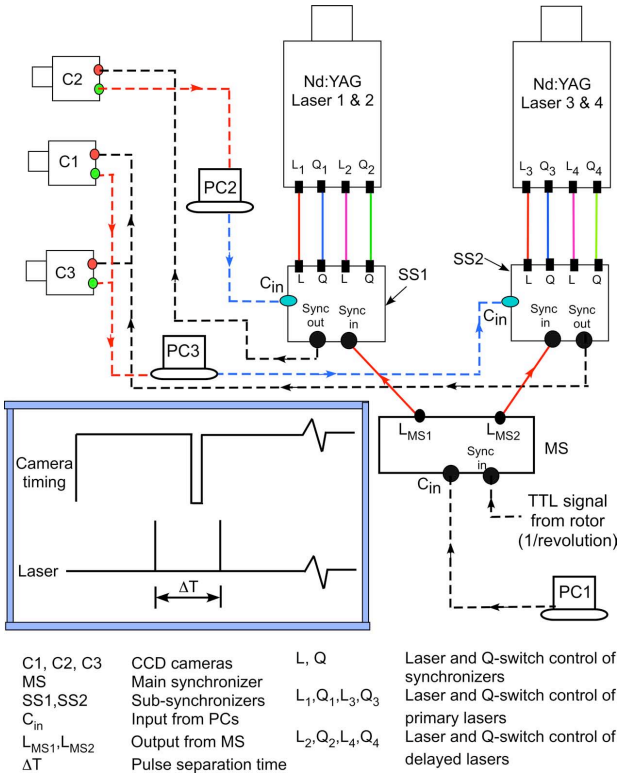

Figure 3: Schematic of the timing circuit for the DPS-DPIV setup.

Coincidence

Another challenge with DPS-DPIV, is the need for coincident flow measurements over each image plane. Even after optically separating the two DPIV systems, both systems must be synchronized so that the flow is measured coincidently in each laser plane. Precise synchronization will guarantee that the flow measurements will be derived from the same flow features, which is absolutely critical for turbulence measurements.

Figure 3 shows the timing diagram used for the present DPS-DPIV experiment, which takes a once-per-revolution pulse signal from the rotor shaft and uses this signal to synchronize the laser pairs with each other and their respective imaging cameras.

DPS-DPIV Particle Image Processing

The digital processing of the acquired images from the cameras used a deformation grid correlation algorithm (see Ref. 31 for details), which is well-optimized for the high velocity gradient flows found in blade tip vortices. The interrogation window size was chosen in such a way that the images from both the cameras were resolved to approximately the same spatial resolution to allow for velocity gradient measurements in the out-of-plane direction.

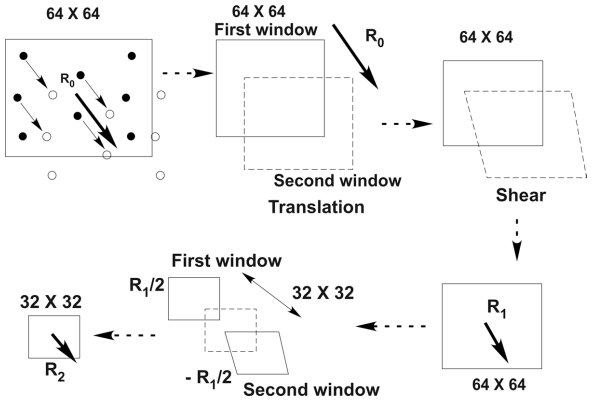

Figure 4: Schematic of the steps involved in the deformation grid correlation.

The steps involved with this correlation algorithm are shown in Fig. 4. The procedure begins with the correlation of an interrogation window of a defined pixel size (e.g., 64-by-64), which is the first iteration. Once the mean displacements in that region are estimated, the interrogation window of the displaced image is moved by integer pixel values for better correlation during the second iteration. The third iteration then moves the interrogation window of the displaced image by sub-pixel values based on the displacements estimated from the second iteration. Following this, the interrogation window is sheared twice (for integer and sub-pixel values) based on the velocity magnitudes from the neighboring nodes, before performing the fourth and fifth iteration, respectively.

Once the velocity is estimated after these five iterations, the original window is split into four equal windows (of pixel size 32×32). These windows are moved by the average displacement estimated from the final iteration (using a pixel window size of 64×64) before starting the first iteration at this resolution. This procedure can be continued until the resolution required to resolve the flow field is reached. The second interrogation window is deformed until the particles remain at the same location after the correlation.

DPS-DPIV Calibration

DPS-DPIV imaging requires a calibration process to incorporate the registration of the cameras and their mappings from the object plane onto the image plane to correct for distortions from variable magnification across the image. For the present system, the single camera and stereo camera pair were mapped in the usual way, followed by the additional step of mapping the cameras to a single reference frame. The latter step was required to map the two separate DPIV grids onto a single grid for gradient calculation between corresponding nodes from the two acquired DPIV velocity vector maps.

A nonlinear mapping function was created from im-

ages of a dual-plane calibration target. This precision calibration target was made from regularly spaced grid of white dots on a black anodized aluminum plate. The resulting mapping function accounts for the image distortion and also provides the third out-of-plane velocity component. The calibration target was mounted on a micrometer-controlled translation stage. A fiducial reference point on the target defined the origin for the calibration images.

Post-Measurement Corrections

In addition to the challenges associated with DPIV image acquisition and image processing (see Ref. 32 for a comprehensive treatment of this issue), there are several post-measurement challenges that can depreciate the accuracy of the measured mean and turbulent flow characteristics. Two of these include: (1) The inherent aperiodicity in the spatial and temporal locations of the blade tip vortices; (2) The inclination of the measurement plane with respect to the rotational axis of the vortex.

Aperiodicity Correction

Making the distinction between mean and turbulent velocity components in the tip vortex is complicated because the wake generally becomes more aperiodic at older ages. This behavior occurs naturally in convecting vortex filaments, which are known to develop various types of self- and mutually-induced instabilities that can be described as "wake modes" (Refs. 24, 33, 34). In successive instantaneous DPIV vector maps, this causes the spatial and temporal locations of the tip vortices to change slightly from one rotor revolution to the next, and so in the images the effect appears as displacements of the vortex center relative to some mean position. Unless this aperiodicity effect is properly and accurately corrected for, it will manifest as a bias in the measurements of both the mean and turbulent flow components.

To first extract accurate mean flow velocities, the positions of the vortices have to be co-located such that the center of each vortex image is perfectly aligned with the center on every other image. This guarantees that the individual mean velocities at a point in the flow are calculated based on spatial locations with respect to a defined tip vortex "center" and are not based on an unadjusted location with respect to the image boundaries. In the present study, the helicity-based aperiodicity bias correction procedure was used, as discussed in detail in Ref. 25.

Mean and turbulence measurements were made from 1,000 instantaneous velocity vector maps, colocating them such that the point of maximum helicity (i.e., the maximum value of the term $\omega_z \cdot w$) coincided before the phase-averaging was conducted. Only after conditional helicity phase-averaging can accurate turbulence properties be estimated.

Measurement Plane Inclination

One further challenge in estimating vortex properties within finite measurement planes is the need to ensure that the measurement planes (as determined by the orientation of the laser light sheets) are orthogonal to the rotational axis of the vortex flow. If the measurement plane is inclined with respect to the vortex axis by more than ten degrees, the planar velocity maps and the resulting vortex properties will be in error.

In previous rotor wake measurements (e.g., Refs. 25, 35, 36), the measurement plane has been aligned so as to be parallel to the rotational axis and also along the 1/4-chord of the blade at a given azimuthal reference angle. Measurements at a given vortex wake age ζ were then made by phase-indexing the rotor blades with respect to this reference plane, and so allowing the vortex wake to be studied as a function of ζ with respect to the reference azimuth. The measurements were performed by assuming that the vortex axis remains normal to the reference plane, regardless of wake age, which has been previously justified because the helicoidal pitch of the wake is low in the hovering state.

To further confirm this parallelity assumption, the orientation of the three-dimensional vorticity vector at the center of the vortex can be calculated directly. This requires the velocity gradients in all three flow directions to calculate the curl of the velocity field. Here, the dual-plane flow measurement technique is especially useful in that all nine velocity gradients in the vortex flow are available.

The measurement plane itself provides the reference from which the velocity gradients are calculated. The vorticity vector can be written as

$$\vec{\omega} = \omega_x \, \hat{i} + \omega_y \, \hat{j} + \omega_z \, \hat{k} \tag{5}$$

where $\hat{i}$, $\hat{j}$, and $\hat{k}$ are unit vectors along the x, y, and z axes of the measurement plane, and ω_x, ω_y, and ω_z are the three components of vorticity, respectively, as given by the curl of the velocity field, i.e.,

$$\begin{aligned} \omega_x &= \partial w/\partial y - \partial v/\partial z \\ \omega_y &= \partial u/\partial z - \partial w/\partial x \\ \omega_z &= \partial v/\partial x - \partial u/\partial y \end{aligned} \tag{6}$$

To find the angle θ between the vorticity vector and the unit normal vector of the measurement plane, $\vec{n}$, the dot product of the two vectors must be calculated. Here, $\vec{n} = 0\hat{i} + 0\hat{j} + 1\hat{k}$, so that

$$\theta = \cos^{-1}\left(\frac{\vec{\omega}\cdot\vec{n}}{|\vec{\omega}|}\right) \tag{7}$$

Wake age, ζ (degrees)	ω_x (1/s)	ω_y (1/s)	ω_z (1/s)	Measurement plane inclination, θ_{MP} (degrees)
4	1907	3864	55212	86
15	2236	5868	57122	84
30	502	4138	54180	87
60	1463	125	36361	88

Table 1: Inclination of the Measurement plane with respect to the vortex axis at four different wake ages.

For a perfectly aligned measurement plane, the normal vector and the vorticity vector should be aligned, i.e., $\theta = 0^\circ$. This alignment corresponds to an 90° angle between the measurement plane and the vortex axis, i.e., $\theta_{MP} = 90^\circ - \theta$.

Calculations for θ_{MP} were performed at four wake ages, and the results are given in Table 1. For the present dual-plane flow experiments, the two laser light sheets (i.e., the two measurement planes) were aligned parallel to the rotational axis and with the 1/4-chord of the blade, as previously described. With this particular setup, the angles θ_{MP} were found to be between 84° and 88°. Therefore, no correction procedure was needed in the present work to account for the inclination of the measurement plane.

Results and Discussion

The results of the current study are discussed in the following categories: (1) Mean flow characteristics and the velocity gradients inside the tip vortices; (2) Turbulence characteristics of the tip vortices. The coordinates (and the sign convention) used in the presentation of the results are shown in Fig. 5.

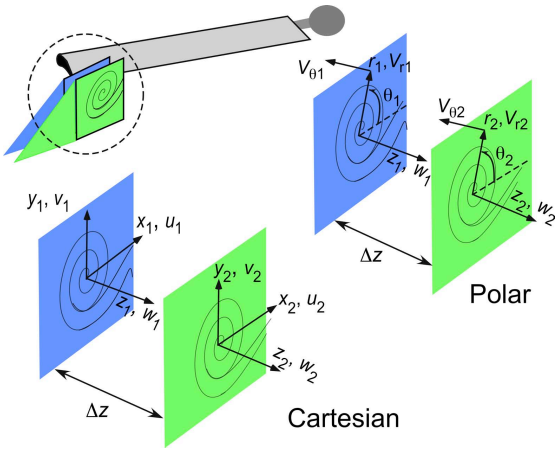

Figure 5: Schematic showing the coordinates systems used for the present experiments.

Mean Tip Vortex Flow Characteristics

After correcting for wake aperiodicity, the DPS-DPIV velocity vector maps were phase-averaged to determine the mean flow characteristics of the tip vortices. As previously described, the determination of the accurate mean flow characteristics of the vortices not only provides an ability to compare vortex characteristics at different wake ages, but is also a prerequisite for accurate turbulence measurements based on Eq. 1.

Representative results of the mean swirl and axial velocity distributions are shown in Figs. 6(a) and 6(b), respectively, and were determined from the measurements

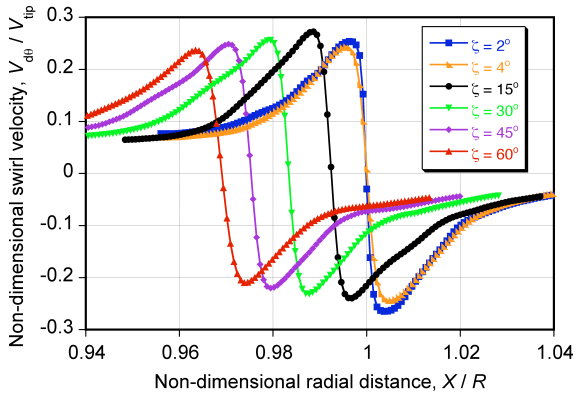

(a) Swirl velocity

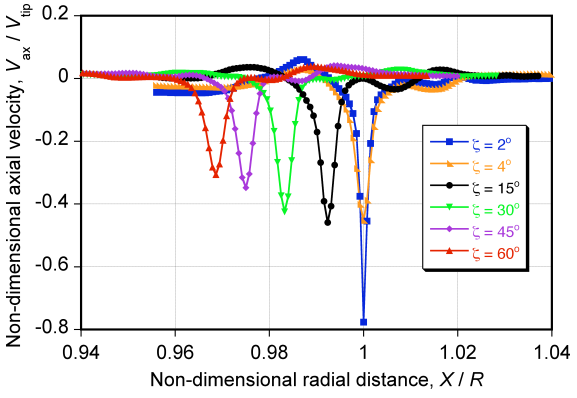

(b) Axial velocity

Figure 6: Normalized swirl and axial velocity distribution at various wake ages: (a) swirl velocity, (b) axial velocity.

by making horizontal slicing cuts across the vortex flow. The classical signature of the swirl velocity distribution can be seen here, with the peak swirl velocity continuously decreasing with increasing wake age as a result of viscous and turbulent diffusion.

In the case of the mean axial velocity, the measurements at the earliest wake age of 2° showed a large deficit of 75% of the blade tip speed. This flow component rapidly reduced to about 45% of tip speed at a wake age of 4°. However, further reductions in the axial velocity proved to be much more gradual, and the peak velocity remained near 30% of the tip speed even after 60° of wake age. Such high values of axial velocity deficit at the centerline of vortices has been previously reported in Ref. 25.

From the swirl velocity profiles, the viscous core radius of the vortex can be estimated. This parameter is usually assumed to be the distance between the center of the vortex (in this case, the point of maximum helicity) and the radial location at which the maximum swirl velocity occurs. In this case, the core size was obtained using the average radial position of the peak velocity found by making a horizontal and vertical cut across the center of the vortex.

Measured core sizes are shown in Fig. 7, along with complementary measurements made using 3-C laser Doppler velocimetry (LDV). The core growth estimated from Squires' model (Ref. 37), as extended by Bhagwat & Leishman (Refs. 38, 39), is given by

$$r_c(\zeta) = \sqrt{r_0^2 + 4\alpha\nu\delta\,(\zeta/\Omega)} \qquad (8)$$

which is also shown in Fig. 7. When $\delta = 1$, this model reduces to the classical Lamb–Oseen model. Increasing values of δ mean that the *average* turbulence levels inside the vortex are higher, which produces more mixing in adjacent fluid layers, faster radial diffusion of vorticity, and consequently a higher average core growth rate with wake age. It can be seen that the present measurements follow the $\delta = 8$ curve, which is also consistent with the LDV measurements.

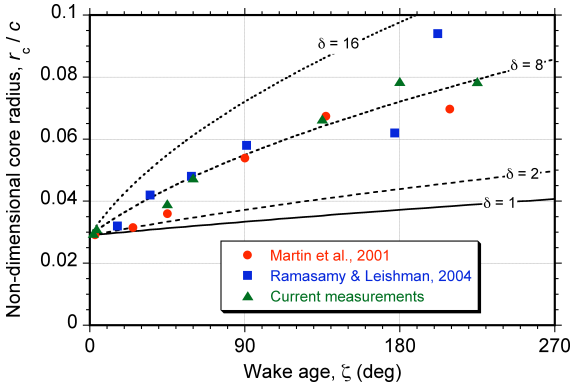

Figure 7: Normalized core growth of the tip vortex as a function of wake age.

Velocity Gradients

As previously described, the corrected mean flow measurements allow for accurate measurements of all nine velocity gradients in the three flow directions. For example, Fig. 8 shows the nine gradients measured at a wake age of 12°. The solid circles marked on each plot represents the average core size of the tip vortex, as estimated by the procedures described previously. The value of the ninth gradient $\partial w/\partial z$ was obtained using the continuity equation given in Eq. 4.

Notice that the gradients of velocity in the plane of measurement (i.e., $\partial/\partial x$ and $\partial/\partial y$) will be referred to the in-plane gradients, and the gradients of velocity orthogonally between the two planes of measurement ($\partial/\partial z$) will be referred to the out-of-plane gradients (refer to Fig. 5 for a visual description).

The results in Fig. 8 show that not only do all these gradients have different orders of magnitude, but their distributions throughout the vortex flow are also different. The presence of the lobed-patterns shown in Fig. 8 are a result of analyzing rotational coherent flow structures in terms of a Cartesian coordinate system (Refs. 16, 40, 41), and are not an artifact of any instrumentation or processing error (Ref. 32). When examining the gradients, both the $\partial u/\partial y$ and $\partial v/\partial x$ components were found to have the highest magnitudes, with both of the components reaching a maximum near the vortex center, albeit with opposite signs.

The in-plane gradients of the axial velocity (i.e., the $\partial w/\partial x$ and $\partial w/\partial y$ terms) were also observed to have large magnitudes near the center; this result can be expected because of the steep rise in the axial velocity deficit within the predominantly viscous vortex core. The two lobes of opposite signs in the distribution pattern of these w gradients, occurs because the velocity deficit increases moving radially inwards toward the center of the vortex, and then decreases when moving radially outwards.

The other in-plane velocity gradients (i.e., the $\partial u/\partial x$ and $\partial v/\partial y$ terms) were observed to exhibit a four-lobed pattern, with the lobes oriented at approximately 45° with respect to the x–y coordinate axes. Specifically, the $\partial u/\partial x$ component showed negative lobes at 45° and 225°, and positive lobes at 135° and 315°. The pattern developed with the $\partial v/\partial y$ gradient was offset from that in $\partial u/\partial x$ by 90°. As a result, when calculating the out-of-plane gradient $\partial w/\partial z$ (whose magnitude is the sum of $\partial v/\partial y$ and $\partial u/\partial x$ based on Eq. 4), the positive lobes in the $\partial u/\partial x$ terms are added to the negative lobes in the $\partial u/\partial x$ terms, and vice-versa. Therefore, these regions tend to cancel each other out, and this leads to the magnitude of $\partial w/\partial z$ being an order of magnitude lower than for the other gradients.

The final two gradients are the out-of-plane gradients of

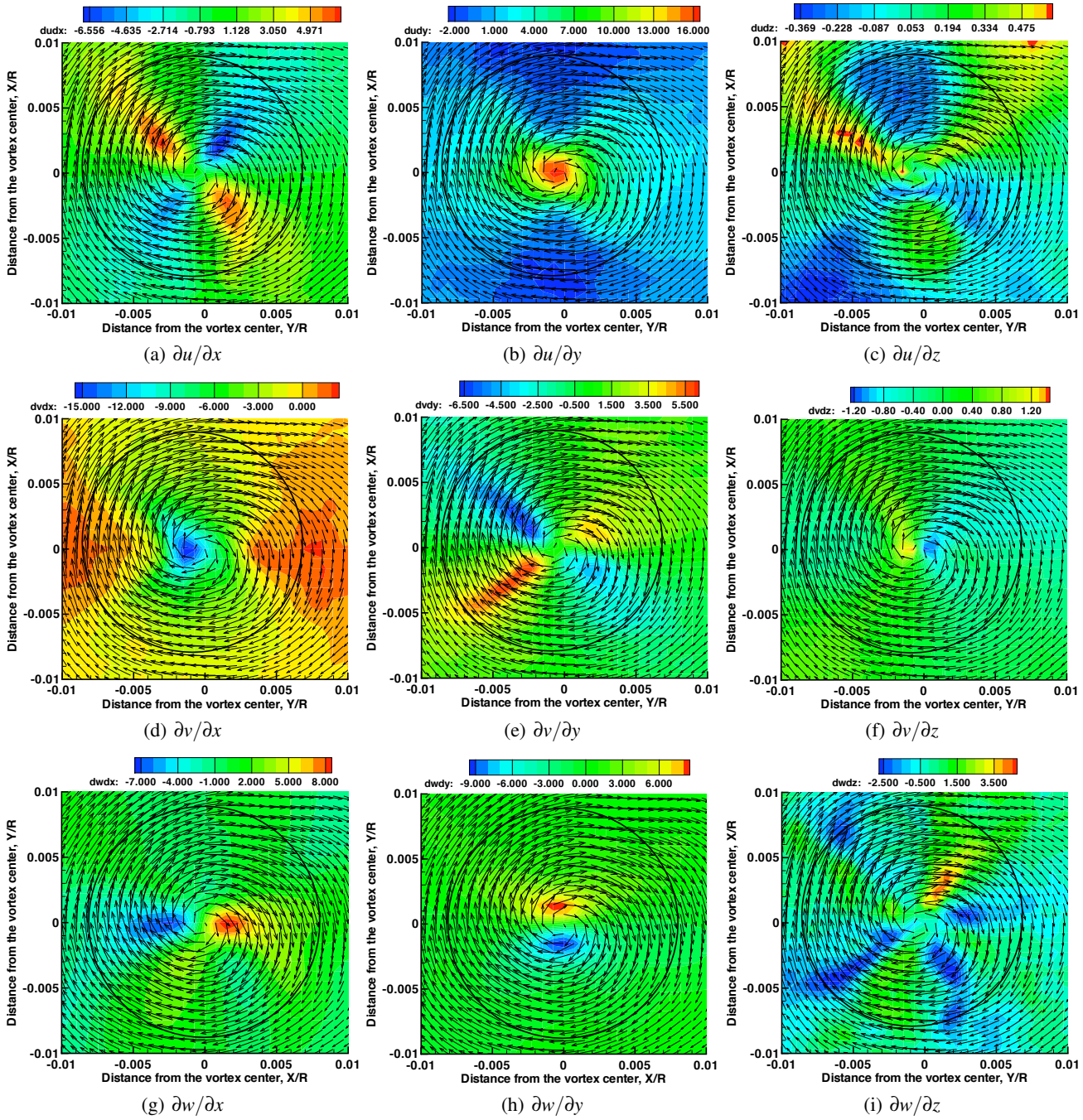

(a) $\partial u/\partial x$ (b) $\partial u/\partial y$ (c) $\partial u/\partial z$

(d) $\partial v/\partial x$ (e) $\partial v/\partial y$ (f) $\partial v/\partial z$

(g) $\partial w/\partial x$ (h) $\partial w/\partial y$ (i) $\partial w/\partial z$

Figure 8: DPS-DPIV measurements of the nine velocity gradients inside the tip vortex core at a wake age of 12°.

the in-plane velocities (i.e., $\partial u/\partial z$ and $\partial v/\partial z$). As might be expected, a two-lobed pattern was observed in each gradient because of the turbulent diffusion of vorticity in the streamwise (or out-of-plane) direction. Based on the coordinate system followed in this work, the $\partial u/\partial z$ term is negative on the lobe aligned with the positive y-axis, and is positive on the lobe aligned with the negative y-axis. This result is consistent with a clockwise rotating vortex when viewed from behind the blade, as is present in the current measurements. In polar coordinates, this means the out-of-plane swirl velocity gradient, $\partial V_\theta/\partial z$, will be negative at all points inside the vortex core, indicating a reduction in the swirl flow of the tip vortices.

Turbulence Characteristics

A detailed analysis was performed on the measured turbulence characteristics to help understand the underlying

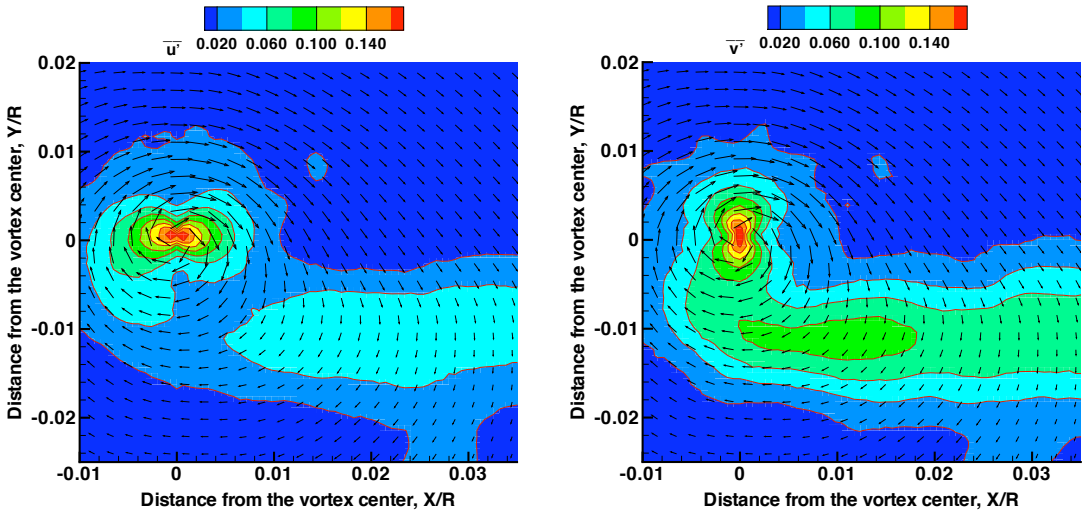

(a) $\zeta = 4^\circ$

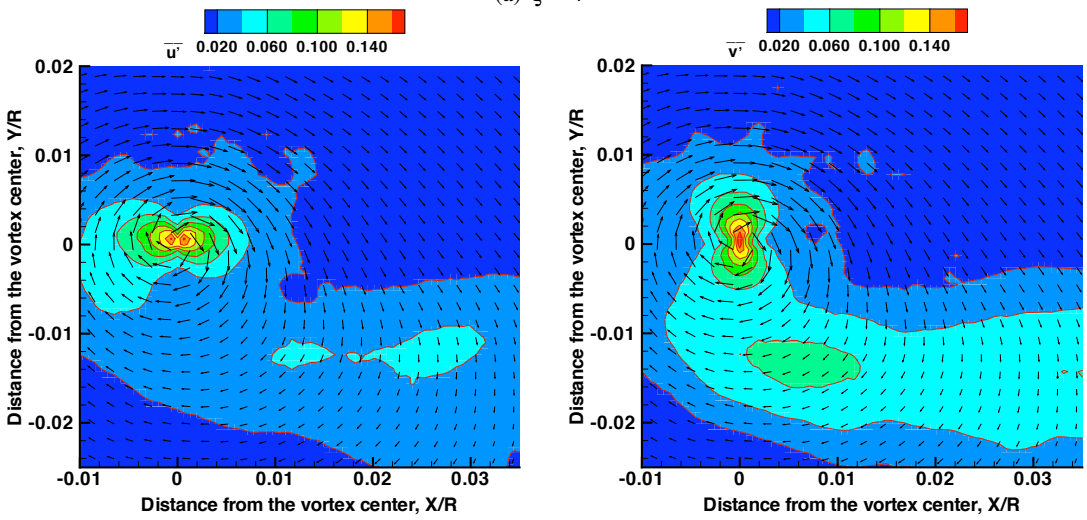

(b) $\zeta = 7^\circ$

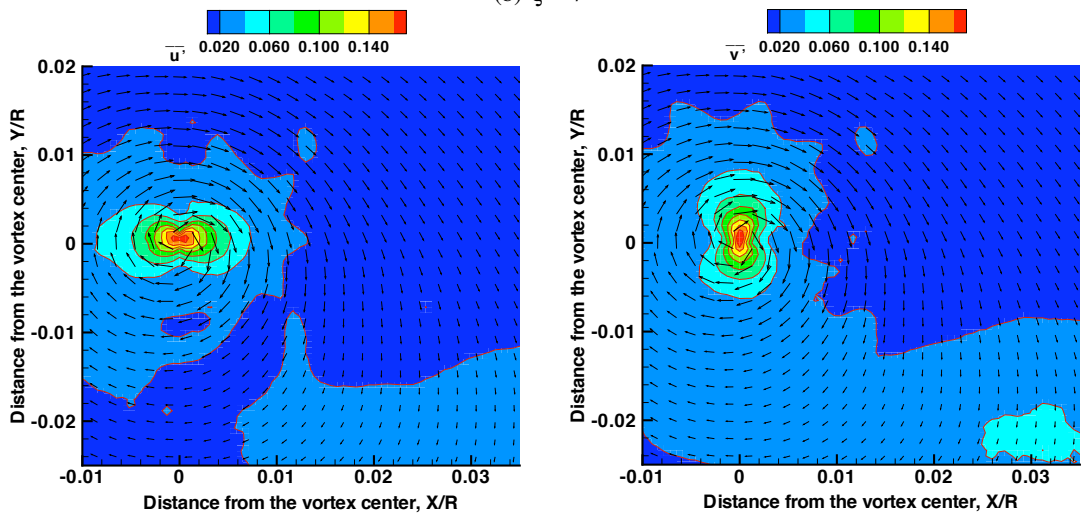

(c) $\zeta = 15^\circ$

Figure 9: In-plane measurements of turbulence right behind the blade over 4° to 15° of wake age: (a) $\zeta = 4^\circ$, (b) $\zeta = 7^\circ$, (c) $\zeta = 15^\circ$. Every fourth vector has been plotted to prevent saturating the image.

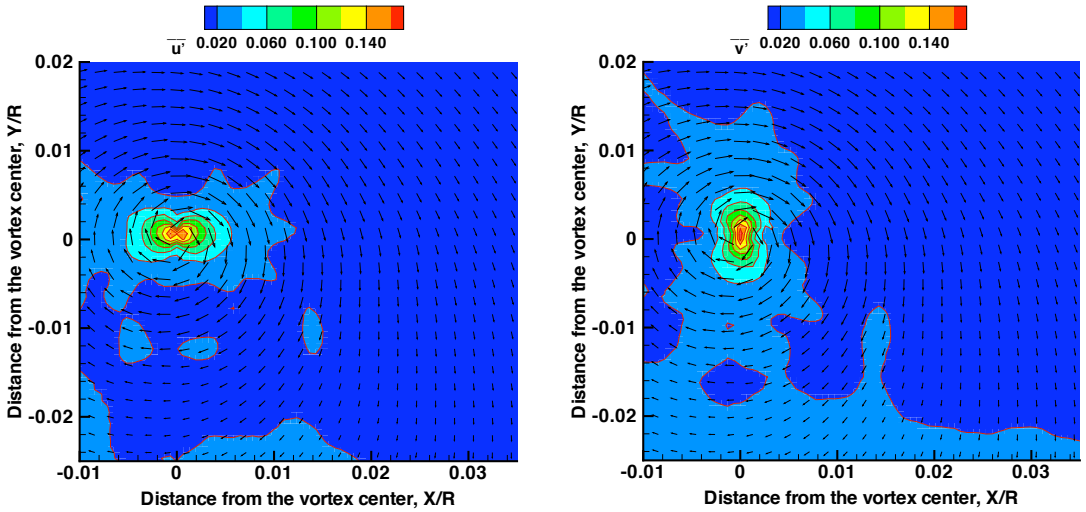

(a) $\zeta = 30^\circ$

Figure 9: (Cont'd) In-plane measurements of turbulence for 30° of wake age: (d) $\zeta = 30^\circ$. Only every fourth vector has been plotted here to prevent saturating the image.

evolutionary behavior of the tip vortices. In the present work, 1,000 instantaneous velocity vector maps were used to estimate the fluctuating velocity components, which is the minimum needed to ensure statistical convergence of the turbulence measurements (Ref. 25).

Notice that in these results, all of the first-order velocity fluctuations were normalized by V_{tip}, and the second-order fluctuations by ${V_{tip}}^2$, respectively, and the length scale was normalized by the blade radius, R. The coordinate axes in each figure are referenced to the phase-averaged center of the vortex, which was defined as the point of maximum helicity as measured at each wake age, as previously described—see Ref. 25 for details.

Turbulence Intensities

Figure 9 shows the distribution of normalized turbulence intensities $\overline{u'}$ and $\overline{v'}$ from $\zeta = 4^\circ$ to 30° of wake age. Notice that a wake age $\zeta = 0^\circ$ corresponds to the point at which the vortex leaves the *trailing-edge* of the blade, not its 1/4-chord. Turbulence measurements were also made around and over the top of the blade surface (i.e., for $\zeta < 0$), thereby capturing the finer details of the vortex formation, and these results are reported in Ref. 16.

It can be seen from Fig. 9, that the $\overline{u'}$ and $\overline{v'}$ components are biased along the x- and y-axes, respectively. This observation is further detailed in Fig. 10, which shows the values of $\overline{u'}$ and $\overline{v'}$ at a wake age of $\zeta = 15^\circ$ that were obtained by making four equi-angle spaced slicing cuts through the center of the vortex. While the $\overline{u'}$ component is the highest along the 0–180 slicing cut (which is a cut along the x-axis of the measurement plane), its magnitude is noticeably smaller along the oblique 45–225 and 135–315 cuts, and the smallest along the 90–270 cut (which is the cut along the y-axis of the measurement plane). Conversely, the $\overline{v'}$ component has the highest magnitude along the 90–270 cut, and the lowest magnitude along the 0–180 cut.

This bias of the velocity fluctuations along their respective axes correlates well with previous turbulence measurements made on a micro-rotor using DPIV (Ref. 25), and also those made behind a fixed-wing using hot wire anemometry (Refs. 40, 41). Despite this bias, notice that both the $\overline{u'}$ and $\overline{v'}$ fluctuations reach a maximum magnitude of approximately equal value at the center of the vortex, and gradually decrease when moving away from its center.

A further perspective into why the turbulent velocity fluctuations were biased along their respective axes in a Cartesian coordinate system analysis is given if the results are transformed into polar coordinates. A representative example is given in Fig. 11, which shows the turbulent fluctuation terms $\overline{V_r'}$ and $\overline{V_\theta'}$ at $\zeta = 15^\circ$ along the same slicing cuts as those used previously in Fig. 10 for the Cartesian analysis. In polar coordinates, it is apparent that there is a much more axisymmetric distribution about the center of the vortex.

This asymmetry can be seen clearly in Fig. 11, which shows that the magnitudes of the $\overline{V_r'}$ and $\overline{V_\theta'}$ components are relatively constant along each slicing cut. This axisymmetric distribution can be shown further if a complete velocity contour map in polar coordinates is made—see Fig. 12 for a wake age of 15°. Unlike the results shown Fig. 9, which clearly shows biased lobes of $\overline{u'}$ and $\overline{v'}$ along the Cartesian axes, the contours in Fig. 12 are almost circular and are centered nicely around the vortex axis.

However, it is apparent the magnitude of the $\overline{V_r'}$ component of turbulence is significantly larger than that of the

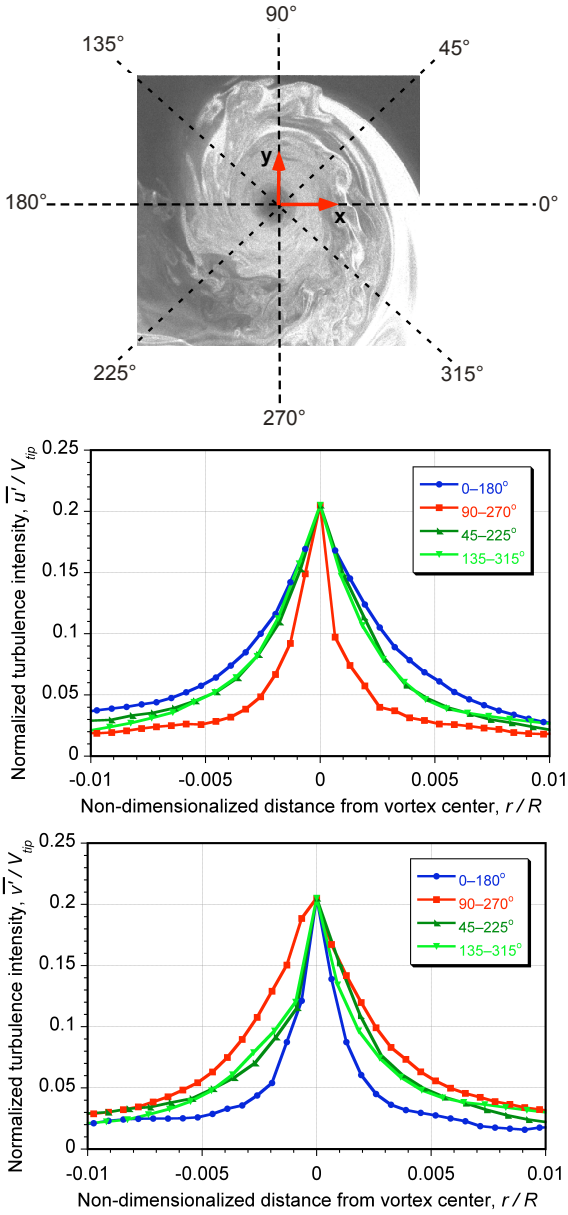

Figure 10: Turbulence fluctuations made in slicing cuts across the vortex at a wake age of 15° in a Cartesian coordinate system.

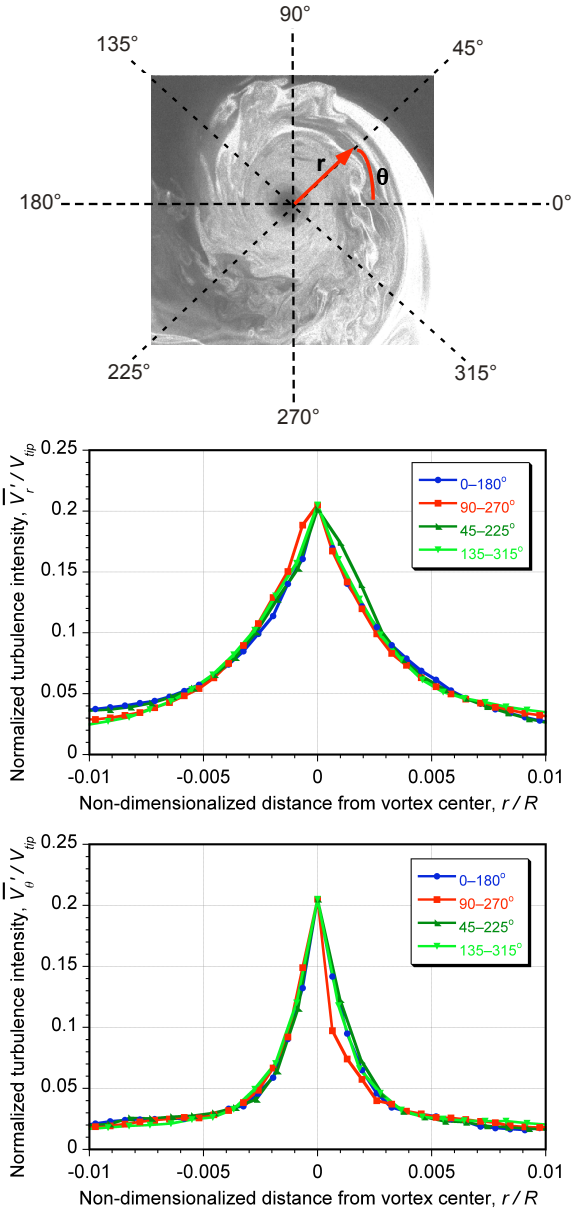

Figure 11: Turbulence fluctuations made in slicing cuts across the vortex at a wake age of 15° in a polar coordinate system.

$\overline{V_\theta'}$ component inside the vortex core. This result is seen in both of the velocity contour plots (Fig. 12) as well as in the one-dimensional slicing cuts through the vortex center (Fig. 13). While both fluctuating terms reach their maximum at the vortex center (as also seen in the Cartesian case in Fig. 10), the $\overline{V_r'}$ turbulence component is larger than $\overline{V_\theta'}$ at all points inside the vortex core. This outcome was found to be the case for all wake ages. This observation is of particular significance in understanding the evolutionary characteristics of vortices, and is an issue that has been previously discussed by Chow et al. (Ref. 41).

Employing this analysis to explain the anisotropy between $\overline{V_r'}$, and $\overline{V_\theta'}$ requires an examination of the turbulence production terms for V_r' and V_θ' transport. The transport equations can be written as

$$V'_{r(\text{prod})} = -2\left[\overline{V_r'^2}\,\frac{\partial V_r}{\partial r} + \overline{V_z'\,V_r'}\,\frac{\partial V_r}{\partial z} - \frac{V_\theta}{r}\,\overline{V_r'\,V_\theta'}\right] \quad (9)$$

$$V'_{\theta(\text{prod})} = -2\left[\overline{V_\theta'^2}\,\frac{\partial V_r}{\partial r} + \overline{V_z'\,V_\theta'}\,\frac{\partial V_\theta}{\partial z} + \frac{\partial V_\theta}{\partial r}\,\overline{V_r'\,V_\theta'}\right] \quad (10)$$

Comparing these two equations shows that the second term in each equation contains the streamwise or out-of-

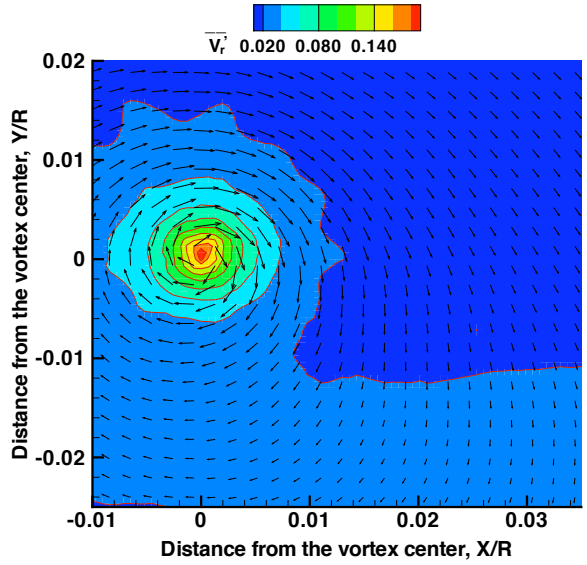

(a) $\overline{V_r'}$

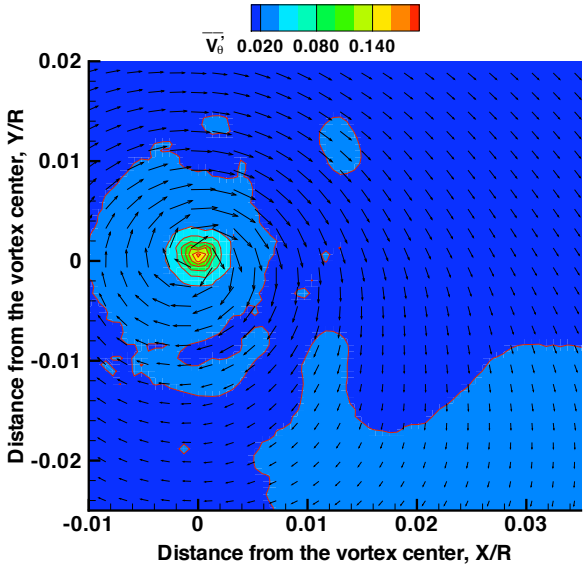

(b) $\overline{V_\theta'}$

Figure 12: Complete velocity contour map of turbulent fluctuation intensities in polar coordinates across the vortex at $\zeta = 15^\circ$: (a) $\overline{V_r'}$ and (b) $\overline{V_\theta'}$.

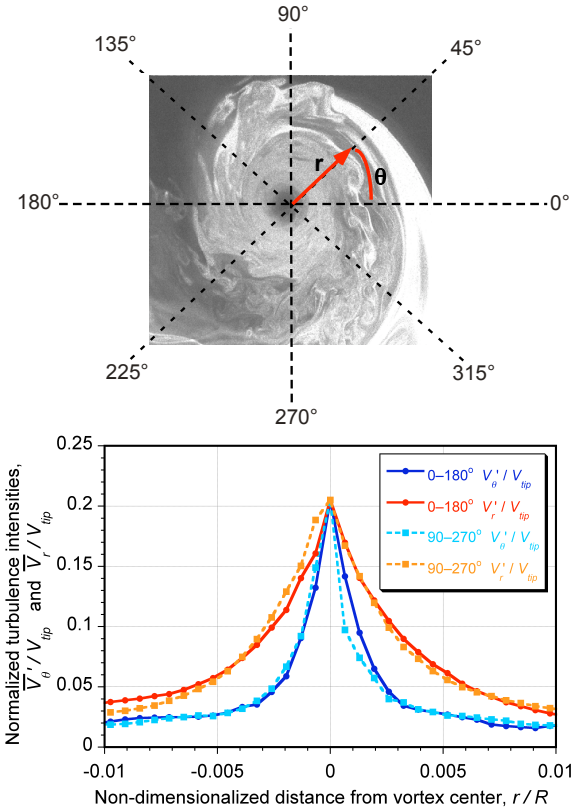

Figure 13: Results showing the anisotropy between $\overline{V_r'}$ and $\overline{V_\theta'}$ across the vortex core at $\zeta = 15^\circ$.

plane gradient. As previously discussed, the magnitude of this term is relatively small and becomes even smaller when multiplied by the shear stress $\overline{V_z'}\,\overline{V_r'}$. The first term in each of the preceding equations is also relatively small. This is because the radial velocity within the vortex flow is very small, making the out-of-plane gradient even smaller. However, the presence of a normal stress term (which is significantly larger than the shear stresses) does tend to compensate for the small gradients found with the radial flow velocity.

The last term in both of the preceding equations involves the shear stress term $\overline{V_r'}\,\overline{V_\theta'}$, as well as the swirl velocity and the velocity gradients. Inside the vortex cores, the components V_θ/r, and $\partial V_\theta/\partial r$ are similar in both sign and magnitude. This is because the swirl velocity rises from zero to a peak swirl velocity in a linear fashion within the viscous core region. This observation is consistent with the assumption of solid-body rotation, which is a good first-order assumption to describe the mean velocities and velocity gradients within the vortex core.

Notice that the assumption of pure solid-body rotation inherently implies that the second-order correlation term $\overline{V_r'V_\theta'}$ has to be identically zero. However, both the present results and those cited in Ref. 41 have measured non-zero values of $\overline{V_r'V_\theta'}$, and predominantly negative values of $\overline{V_r'}\,\overline{V_\theta'}$ within the vortex core. A non-zero, negative value of $\overline{V_r'V_\theta'}$ will increase the production of $\overline{V_r'}$ and reduce $\overline{V_\theta'}$ because of the sign difference between the last terms of Eq. 9 and Eq. 10. Consequently this will result in the $\overline{V_r'}$ component being greater than $\overline{V_\theta'}$, thereby leading to an anisotropic distribution of turbulence within the vortex flow. Converting this anisotropy from polar to Cartesian coordinates will then produce the intensity bias observed in the $\overline{u'}$ and $\overline{v'}$ components, as shown previously in Fig. 9.

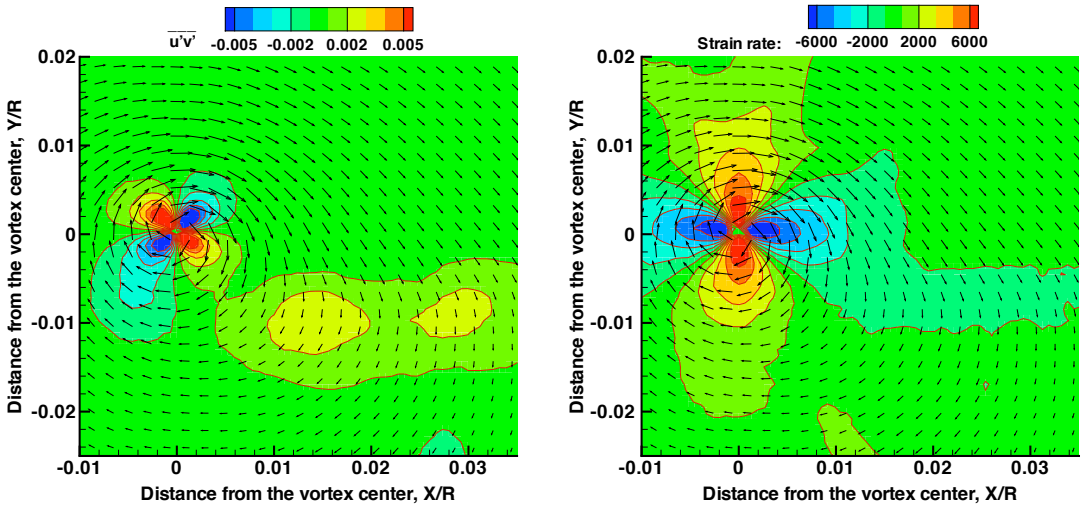

(a) $\zeta = 4^\circ$

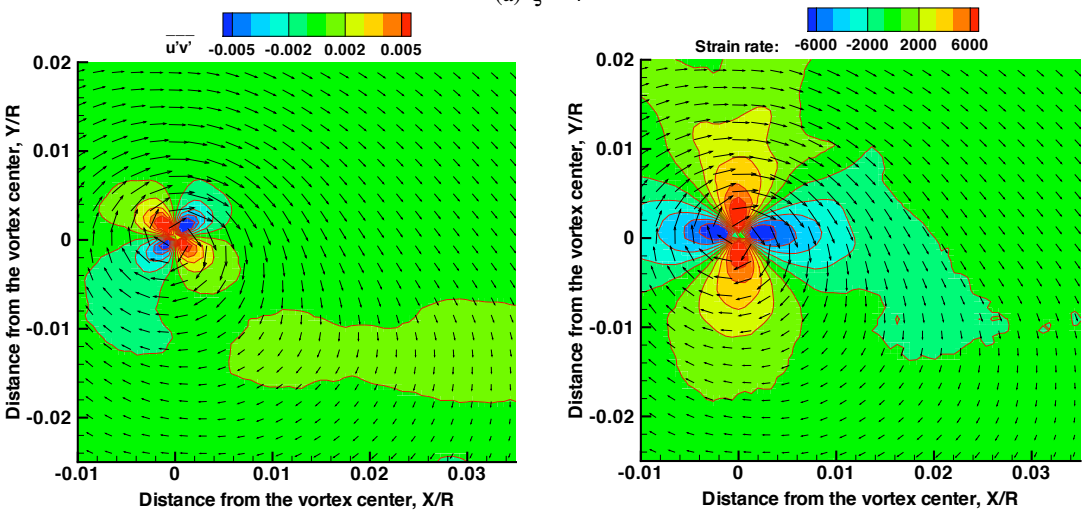

(b) $\zeta = 7^\circ$

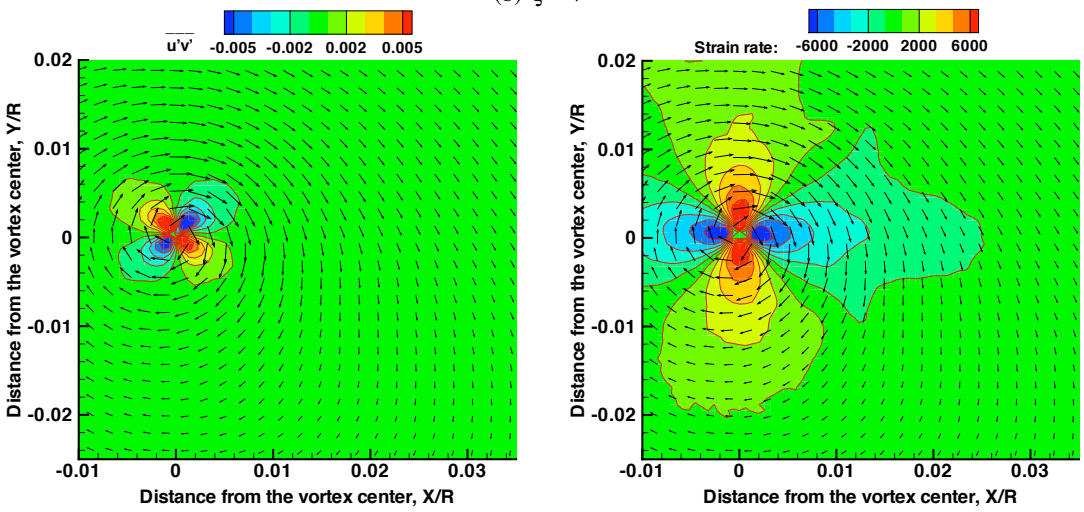

(c) $\zeta = 15^\circ$

Figure 14: In-plane measurements of Reynolds stress and strain behind the blade over 4° to 15° of wake age: (a) $\zeta = 4^\circ$, (b) $\zeta = 7^\circ$, (c) $\zeta = 15^\circ$.

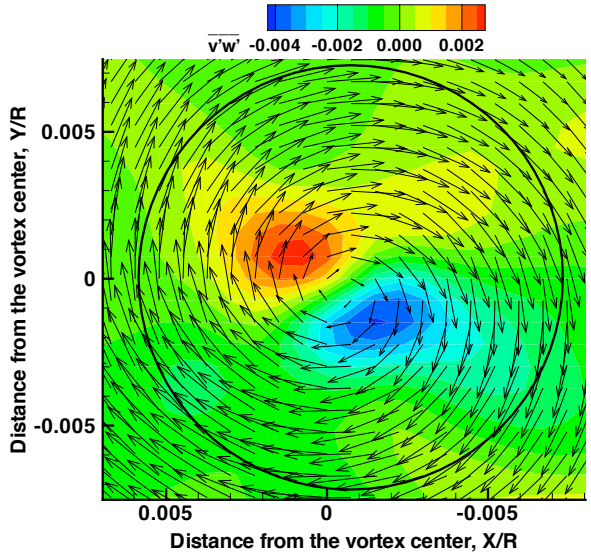

(a) $\overline{v'w'}$ at $\zeta = 60^\circ$

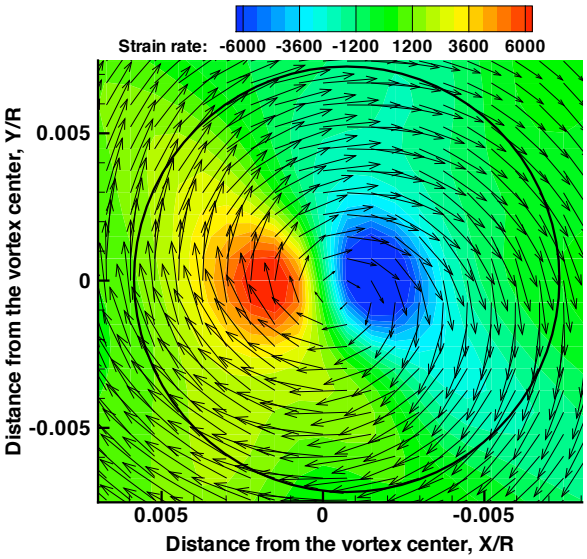

Figure 15: Reynolds stress and strain rate at 60° of wake age showing an anisotropy in their distributions: (a) Stress $\overline{v'w'}$, (b) Strain rate $-(\frac{\partial v}{\partial z} + \frac{\partial w}{\partial y})$.

Reynolds Stresses

Figure 14 shows the distribution of the Reynolds shear stress ($\overline{u'v'}$) and the associated strain ($\partial u/\partial y + \partial v/\partial x$) measured from wake ages of $\zeta = 4^\circ$ to $\zeta = 15^\circ$. The reason for showing shear stress and strain together is because of the basic assumption made in eddy viscosity-based turbulence models that stress is a *linear* function of strain. However, even a cursory examination of the contours in Fig. 14 clearly suggests that this assumption is invalid, as has already been shown for flows with highly curved streamlines (Refs. 42, 43).

Figure 14 shows that the shear stress and strain quickly form sharp, four-lobbed patterns as early as $\zeta = 4^\circ$. These lobes, whose magnitudes alternate in sign, are aligned along the Cartesian coordinate axes for strain, and at a 45° angle with respect to the coordinate axes for the shear stress. The contours also suggest significantly high levels of shear stress inside the vortex sheet at early wake ages, which can be expected based on results of the instantaneous turbulence activity shown in the results of Ref. 16.

The present DPS-DPIV system also allows for the measurement of the $\overline{v'w'}$ component of the Reynolds shear stress and its associated strain. These results are plotted in Fig. 15 for $\zeta = 60^\circ$. Unlike the $\overline{u'v'}$ term, the $\overline{v'w'}$ term has only two lobes. However, the alignment of these lobes are still at a 45° offset angle from the coordinate axes.

The associated strain also shows only two lobes, which are aligned with the x-axis. This suggests that the orientation of all the shear stress distributions are again at a 45° offset from the shear strain distribution. Notice that this conclusion has also been drawn in Ref. 41 based on experiments with vortices generated by a fixed-wing, and also in Ref. 25 based on vortex flows generated by microrotor, albeit at much smaller vortex Reynolds numbers. Therefore, the evidence suggests that the common modeling assumption that stress is a linear function of strain is invalid for vortex flows.

Turbulent Transport and Vortex Evolution

One effective way to correlate the core growth of the tip vortex (see Fig. 7) and the production of turbulence, is through comparisons of the distributions of the eddy viscosity across the core. Any growth of the vortex core depends on the diffusion of momentum from one layer in the fluid to an adjacent layer. This process depends on the eddy viscosity, which in turn is a function of the shear stress (i.e., Boussinesq's assumption—see Ref. 44).

Figure 16 shows the measured Reynolds shear stress $\overline{u'v'}$ in the tip vortex for three wake ages. It is clear that the peak value of the shear stress decreases with wake age,

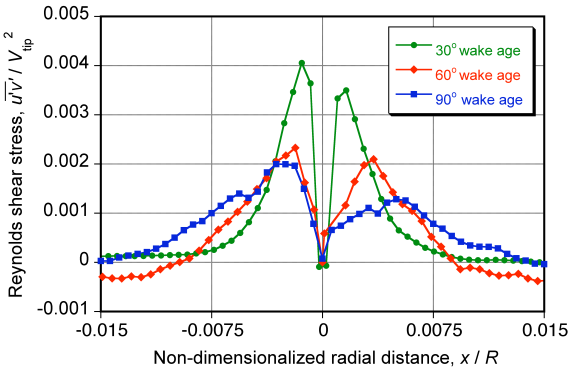

Figure 16: Reynolds stress ($\overline{u'v'}$) distribution at three wake ages.

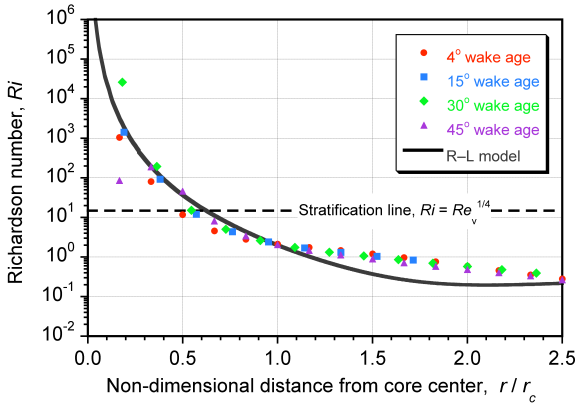

Figure 17: The variation of the Richardson number across the vortex suggests that turbulence production will be suppressed in the central core region. Measurements made at $\zeta = 4°$, 15°, 30° and 45°.

and is also progressively distributed further away from the vortex center. While the peak values of shear stress move radially further away from the core at the older ages, the area under the curves still remain approximately constant. This means that the *average* eddy viscosity is also approximately constant, which is the basic assumption made in the core growth models of Bhagwat & Leishman (Refs. 38, 39) and Ramasamy & Leishman (Ref. 45).

The existence of the eddy viscosity is the basic fluid mechanics phenomenon that will sustain the growth rate of the vortex cores. In the Ramasamy–Leishman (R–L) turbulence model (Ref. 45), a Richardson number (*Ri*) concept is used to describe the resulting distribution of eddy viscosity as a function of vortex Reynolds number. The *Ri* is the ratio of turbulence produced or consumed from the centrifugal force to turbulence produced from shear (Refs. 42, 46, 47) and is given by

$$Ri = \left(\frac{2V_\theta}{r^2}\frac{\partial(V_\theta r)}{\partial r}\right) \Big/ \left(r\frac{\partial(V_\theta/r)}{\partial r}\right)^2 \qquad (11)$$

Turbulence produced by shear is usually very low at the center of the vortex (pure solid body rotation does not produce any turbulence at all because there is no shear). Consequently, the value of *Ri* is high near the center of the vortex, and is much larger than the threshold value that allows for the sustainment of turbulence—see Fig. 17. This threshold is based on the attainment of a critical value of vortex Reynolds number (Refs. 46, 47). Therefore, turbulence is neither produced nor easily sustained near the center of a vortex, a result also suggested by flow visualization, as shown in Fig. 18.

Turbulence production can be calculated by finding the product of the strain rate and the Reynolds shear stress. The mean strain for a given vortex is defined, so the production depends largely on the shear stress. Because it can

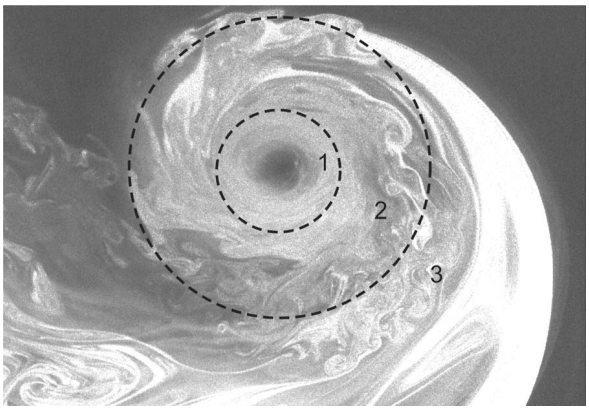

Figure 18: Flow visualization of a fully-developed blade tip vortex: 1. Inner, almost laminar zone free of turbulent eddies, 2. A transitional region with various eddies of different scales, and 3. An outer flow region.

be seen in Fig. 16 that the shear stress is a minimum at the center of the vortex, the intermittency function given in the R–L turbulence model (Ref. 45) is, therefore, fully consistent with the findings made with the present set of measurements.

In addition to the radial core growth of the vortex, the axial velocity inside the vortex is also dependent upon the Reynolds stresses. This result can be better understood from an examination of the scalar momentum equation in the z direction, which is given by

$$u\frac{\partial u}{\partial z} + v\frac{\partial v}{\partial z} + w\frac{\partial w}{\partial z} = -\frac{1}{\rho}\frac{\partial p}{\partial z} + \nu\nabla^2 w - \frac{\partial \overline{u'w'}}{\partial x} - \frac{\partial \overline{v'w'}}{\partial y} - \frac{\partial \overline{w'^2}}{\partial z} \qquad (12)$$

The pressure gradient in Eq. 12, which is positive during the tip vortex roll-up process (resulting in an increased axial velocity deficit as the wake age increases), can be assumed to be negligible at older wake ages. Similarly, the effects of molecular viscosity alone can be considered to be negligible compared to the effects of the turbulent (eddy) viscosity. This leaves the gradients of the stress terms (i.e., $\overline{u'w'}$, $\overline{v'w'}$, and $\overline{w'^2}$) to play a role in defining the axial momentum. This behavior is especially important at the center of the vortex flow, where the axial velocity deficit reaches its maximum.

The results shown in Fig. 15(b) suggests that the gradients $\partial\overline{v'w'}/\partial y$ are relatively high inside the vortex core. Such high gradients directly transfer momentum from the streamwise direction to the cross flow direction, thereby resulting in a reduction of the peak axial velocity, as shown previously in Fig. 6(b).

Conclusions

Velocity field and turbulence measurements were made in the wake of a hovering rotor using dual-plane digital particle image velocimetry (DPS-DPIV). The DPS-DPIV technique allowed for the measurement of the three instantaneous flow velocity components, as well as all nine-components of the velocity gradient tensor, a capability not possible with conventional DPIV systems. The method was based on coincident flow measurements made over two differentially spaced laser sheet planes. A polarization-based approach was used in which the two laser sheets were given orthogonal polarizations, with filters and beam-splitting optical cubes placed so that the imaging cameras saw Mie scattering from only one or other of the laser sheets. The digital processing of the acquired images was based on a deformation grid correlation algorithm that was optimized to measure the high velocity gradients and turbulent flows found inside vortices.

The following are the main conclusions drawn from this study:

1. The measured peak axial velocity deficit (corrected for aperiodicity bias effects using a helicity-based method) was found to be about 75% of the tip speed at the earliest wake age behind the blade. This axial velocity remained as high as 40% as late as 60° of wake age. Mean flow measurements inside the tip vortices showed that the radial diffusion of vorticity as a result of turbulence generation was about eight times higher than than would be expected for a fully laminar flow. This finding is consistent with previous measurements of vortex core growth.

2. Turbulence intensity measurements inside the tip vortices clearly showed an anisotropy. Specifically, the $\overline{V_r}'$ turbulence component was found to be greater in magnitude than the $\overline{V_\theta}'$ component at all points inside the vortex flow. This anisotropy, in turn, radially biases the velocity fluctuations in $\overline{u'}$ and $\overline{v'}$ when viewed in a Cartesian coordinate system. In polar coordinates, the $\overline{V_r'}$ turbulence component was found to be larger than $\overline{V_\theta'}$ at all points inside the vortex core.

3. While the assumption of solid body rotation inside the vortex core is a reasonable assumption for first principles-based modeling of tip vortices, it falls short in predicting the second-order velocity fluctuations that are used in the Reynolds-averaged stress transport equations. Specifically, the $\overline{V_r'V_\theta'}$ term was found to be predominantly negative in the present measurements.

4. The results confirm that the shear stresses in blade tip vortices cannot be written as a linear function of strain, as assumed in existing linear eddy viscosity based turbulence models. Obviously, further work must be done to develop more appropriate turbulence models if the goal is to improve predictions of the rotor wake, and to predict accurately the loads from vortex-wake induced phenomena.

Acknowledgments

This research was partly supported by the Army Research Office (ARO) under grant W911NF0610394 and partly under the Multi-University Research Initiative under Grant W911NF0410176. Dr. Thomas Doligalski was the technical monitor for both contracts. The authors would like to thank Drs. Christopher Cadou and Kenneth Yu for loaning the additional lasers needed for this work. Our appreciation also extends to Joseph Ramsey, who aided in the processing of the DPIV data and in the analysis of the flow measurements.

References

[1]Drees, J. M., and Hendal, W. P., "The Field of Flow Through a Helicopter Rotor Obtained from Wind Tunnel Smoke Tests," *Journal of Aircraft Engineering*, Vol. 23, (266), February 1950, pp. 107–111.

[2]Landgrebe, A. J., "An Analytical Method for Predicting Rotor Wake Geometry," AIAA/AHS VTOL Research, Design & Operations Meeting, Atlanta, GA, February 1969.

[3]Cook, C. V., "The Structure of the Rotor Blade Tip Vortex," Paper 3, Aerodynamics of Rotary Wings, AGARD CP-111, September 13–15, 1972.

[4]Tung, C., Pucci, S. L., Caradonna, F. X., and Morse, H. A., "The Structure of Trailing Vortices Generated by Model Helicopter Rotor Blades," NASA TM 81316, 1981.

[5]Egolf, T. A., and Landgrebe, A. J., "Helicopter Rotor Wake Geometry and its Influence in Forward Flight, Vol. 1 – Generalized Wake Geometry and Wake Effects in Rotor Airloads and Performance," NASA CR-3726, October 1983.

[6]Johnson, W., "Wake Model for Helicopter Rotors in High Speed Flight," NASA CR-1177507, USAVSCOM TR-88-A-008, November 1988.

[7]Leishman, J. G., and Bi, N., "Measurements of a Rotor Flowfield and the Effects on a Body in Forward Flight," *Vertica*, Vol. 14, (3), 1990, pp. 401–415.

[8]Lorber, P. F., Stauter, R. C., Pollack, M. J., and Landgrebe, A. J., "A Comprehensive Hover Test of the Airloads and Airflow of an Extensively Instrumented Model Helicopter Rotor," Vol. 1–5, USAAVSCOM TR-D-16 (A-E), October 1991.

[9]Bagai, A., Moedersheim, E., and Leishman, J. G., "Developments in the Visualization of Rotor Wakes using the Wide-Field Shadowgraph Method," *Journal of Flow Visualization & Image Processing*, Vol. 1, (3), July–September 1993, pp. 211–233.

[10]Bhagwat, M. J., and Leishman, J. G., "Stability Analysis of Helicopter Rotor Wakes in Axial Flight, *Journal of the American Helicopter Society*, Vol. 45, (3), July 2000, pp. 165–178.

[11]Bagai, A., and Leishman, J. G., "Flow Visualization of Compressible Vortex Structures Using Density Gradient Techniques," *Experiments in Fluids*, Vol. 15, (6), October 1993, pp. 431–442.

[12]McAlister, K. W., "Measurements in the Near Wake of a Hovering Rotor," 27th AIAA Fluid Dynamic Conference Proceedings, New Orleans, June 18–20, 1996.

[13]Leishman, J. G., Han, Y. O., and Coyne, A. J., "Measurements of the Velocity and Turbulence Structure of a Rotor Tip Vortex," *AIAA Journal*, Vol. 35, (3), March 1997, pp. 477–485.

[14]Martin, P. B., and Leishman, J. G., "Trailing Vortex Measurements in the Wake of a Hovering Rotor with Various Tip Shapes," American Helicopter Society 58th Annual National Forum Proceedings, Montréal Canada, July 11–13, 2002.

[15]Ramasamy, M., and Leishman, J. G., "Interdependence of Diffusion and Straining of Helicopter Blade Tip Vortices," *Journal of Aircraft*, Vol. 41, (5), September 2004, pp. 1014–1024.

[16]Ramasamy, M., Johnson, B., and Leishman, J. G., "Tip Vortex Measurements Using Dual Plane Digital Particle Image Velocimetry," American Helicopter Society 64th Annual National Forum Proceedings, Montréal Canada, April 28–30, 2008.

[17]Johnson, D. A., and King, L. S., "A Mathematically Simple Trubulence Closure Model for Attached and Separated Turbulent Boundary Layers," *AIAA Journal*, Vol. 23, 1985, pp. 1684–1692.

[18]Durbin, P. A., "Near-Wall Turbulence Closure Modelling Without Damping Functions," *Journal of Theoretical Computational Fluid Dynamics*, Vol. 3, 1991, pp. 1–13.

[19]Baldwin, B. S., and Lomax, P. S., "Thin Layer Approximation and Algebraic Model for Separated Turbulent Flows," AIAA Paper 78-0257, 16th AIAA Aerospace Sciences Meeting and Exhibit, Huntsville, AL, January 1978, AIAA.

[20]Spalart, P. R., and Allmaras, S. R., "A One-Equation Turbulence Model for Aerodynamic Flows," AIAA Paper 92-0439, 30th AIAA Aerospace Sciences Meeting & Exhibit, January 1992.

[21]Baldwin, B. S., and Barth, T. J., "A One Equation Turbulence Transport Model for High Reynolds Number Wall Bounded Flows," NASA TM 102847, 1990.

[22]Leishman, J. G., "On Seed particle Dynamics in Tip Vortex Flows," *Journal of Aircraft*, Vol. 33, (4), July/August 1996, pp. 823–825.

[23]Martin, P. B., Bhagwat, M. J., and Leishman, J. G., "Strobed Laser-Sheet Visualization of a Helicopter Rotor Wake," Paper PF118, Proceedings of PSFVIP-2, Honolulu, HI, May 1999. See also: Martin, P. B., Bhagwat, M. J., and Leishman, J. G., "Strobed Laser Sheet Visualization of a Helicopter Rotor Wake," *Journal of Flow Visualization and Image Processing*, Vol. 7 (1), 2002 pp. 31–50.

[24]Bhagwat, M. J., and Leishman, J. G., "On the Stability of the Wake of a Rotor in Axial Flight," American Helicopter Society 56th Annual National Forum Proceedings, Virginia Beach, VA, May 2–4, 2000.

[25]Ramasamy, M., Johnson, B., Huismann, T., and Leishman, J. G., "A New Method for Estimating Turbulent Vortex Flow Properties from Stereoscopic DPIV Measurements," American Helicopter Society 63rd Annual National Forum Proceedings, Virginia Beach, VA, May 1–3, 2007.

[26]Raffel, M., Richard, H., Ehrenfried, K., van der Wall, B. G., Burley, C. L., Beaumier, P., McAlister, K. W., and Pengel, K., "Recording and Evaluation Methods of PIV Investigations on a Helicopter Rotor Model," *Experiments in Fluids*, Vol. 36, 2004, pp. 146–156.

[27]Heineck, J. T., Yamauchi, G. K., Wadcock, A. J., Lourenco, L., and Abrego, A. I., "Application of Three-Component PIV to a Hovering Rotor Wake," American Helicopter Society 56th Annual National Forum Proceedings, Virginia Beach, VA, May 2–4, 2000.

[28]van der Wall, B. G., and Richard, H., "Analysis Methodology for 3C-PIV Data of Rotary Wing Vortices," *Experiments in Fluids*, Vol. 40, 2006, pp. 798–812.

[29]Hu, H., Saga, T., Kobayashi, N., Taniguchi, N., and Yasuki, M., "Dual-Plane Stereoscopic Particle Image Velocimetry: System Set-up and Its Application On a Lobed Jet Mixing Flow," *Experiments in Fluids*, Vol. 33, September 2001, pp. 277–293.

[30]Ganapathisubramani, B., Longmire, E. K., Marusic, I., and Stamatios, P., "Dual-plane PIV Technique to Determine the Complete Velocity Gradient Tensor in a Turbulent Boundary Layer," *Experiments in Fluids*, Vol. 39, August 2005, pp. 222–231.

[31]Scarano, F., "Iterative Image Deformation Methods in PIV," *Measurement Science and Technology*, Vol. 13, 2002, pp. R1–R19.

[32]Ramasamy, M., and Leishman, J. G., "Benchmarking PIV with LDV for Rotor Wake Vortex Flows," *AIAA Journal*, Vol. 45, (11), November 2007, pp. 2622–2633.

[33]Tangler, J. L., Wohlfeld, R. M., and Miley, S. J., "An Experimental Investigation of Vortex Stability, Tip Shapes, Compressibility, and Noise for Hovering Model Rotors," NASA CR-2305, September 1973.

[34]Leishman, J. G., "On the Aperiodicity of Helicopter Rotor Wakes," *Experiments in Fluids*, Vol. 25, 1998, pp. 352–361.

[35]Martin, P. B., Pugliese, G., and Leishman, J. G., "High Resolution Trailing Vortex Measurements in the Wake of a Hovering Rotor," American Helicopter Society 57th Annual National Forum Proceedings, Washington, DC, May 9–11, 2001.

[36]Duraisamy, K., Ramasamy, M., Baeder, J. D., and Leishman, J. G., "High Resolution Computational and Experimental Study of Rotary Wing Tip Vortex Formation," *AIAA Journal*, Vol. 45, (11), November 2007, pp. 2593–2602.

[37]Squire, H. B., "The Growth of a Vortex In Turbulent Flow," *Aeronautical Quarterly*, Vol. 16, August 1965, pp. 302–306.

[38]Bhagwat, M. J., and Leishman, J. G., "Measurements of Bound and Wake Circulation on a Helicopter Rotor," *Journal of Aircraft*, Vol. 37, (2), 2000.

[39]Bhagwat, M. J., and Leishman, J. G., "Correlation of Helicopter Tip Vortex Measurements," *AIAA Journal*, Vol. 38, (2), February 2000, pp. 301–308.

[40]Chow, J. S., Zilliac, G. G., and Bradshaw, P., "Measurements in the Near-Field of a Turbulent Wingtip Vortex," Paper AIAA-93-0551, 31st Aerospace Sciences Meeting & Exhibit, Reno, NV, January 11–14, 1993.

[41]Chow, J. S., Zilliac, G. G., and Bradshaw, P., "Mean and Turbulence Measurements in the Near Field of a Wingtip Vortex," *AIAA Journal*, Vol. 35, (10), October 1997, pp. 1561–1568.

[42]Bradshaw, P., "The Analogy Between Streamline Curvature and Buyoyancy in Turbulent Shear Flows," *Journal of Fluid Mechanics*, Vol. 36, (1), March 1969, pp. 177–191.

[43]Zilliac, G. G., Chow, J. S., Dacles-Mariani, J., and Bradshaw, P., "Turbulent Structure of a Wingtip Vortex in the Near Field," Paper AIAA-93-3011, 24th AIAA Fluid Dynamic Conference Proceedings, Orlando, FL, July 6–9 1993.

[44]Boussinesq, J., "Essai sur la théorie des eaux courantes, Mémoires présentés par divers à la Académie des Sciences" XXIII, 1, 1877, pp. 1–680.

[45]Ramasamy, M., and Leishman, J. G., "A Generalized Model for Transitional Blade Tip Vortices," *Journal of the American Helicopter Society*, Vol. 51, (1), January 2006, pp. 92–103.

[46]Cotel, A. J., and Breidenthal, R. E., "Turbulence Inside a Vortex," *Physics of Fluids*, 11 (10), 1999, pp. 3026–3029.

[47]Cotel, A. J., "Turbulence Inside a Vortex: Take Two," *Physics of Fluids*, 14 (8), 2002, pp. 2933–2934.